ACS APPLIED MATERIALS & INTERFACES

www.acsami.org

Research Article

Confining Ultrafine MoO_2 in a Carbon Matrix Enables Hybrid Li Ion and Li Metal Storage

Yao Yao,[‖] Ziang Chen,[‖] Ruohan Yu, Qiang Chen, Jiexin Zhu, Xufeng Hong, Liang Zhou,* Jinsong Wu,* and Liqiang Mai*

Cite This: *ACS Appl. Mater. Interfaces* 2020, 12, 40648−40654

Read Online

ACCESS | Metrics & More | Article Recommendations | Supporting Information

ABSTRACT: Poor cycle and rate performance caused by volume effects and sluggish kinetics is the main bottleneck for most lithium-ion battery (LIB) anode materials run on the conversion reaction. Although nanostructure engineering has shown to be an effective method to reduce the undesirable volume effects, cycling instability usually remains in nanostructured electrodes owning to particle aggregation in discharge and loss of active materials in charge. Here, to make these kinds of materials practical, we have developed a structure of ultrafine MoO_2 nanoparticles (<3 nm) confined by a conductive carbon nanosheet matrix (MoO_2/C). Instead of running on the conversion mechanism, the Li storage in the MoO_2/C composite is through a two-step mechanism in discharge: intercalation followed by the formation of metallic Li, acting as a hybrid host for both Li ion intercalation and metallic Li plating. The Li-storage mechanism has been revealed by *in situ* X-ray diffraction analysis and *in situ* scanning transmission electron microscopy with corresponding electron energy loss spectrum analysis, which explains the natural origin of such high capacity along with good cyclability. This unique MoO_2/C structure exhibits an excellent discharge capacity (810 mAh g^{-1} at 200 mA g^{-1}) and cyclability (75% capacity retention over 1000 cycles). The carbon sheet plays a vital role in both a conductive network and a structure supporter with a robust confining effect that keeps the size of MoO_2 uniformly under 3 nm even after high-temperature calcination. Our finding provides insights for the design of next-generation LIB anode materials with high capacity and longevity.

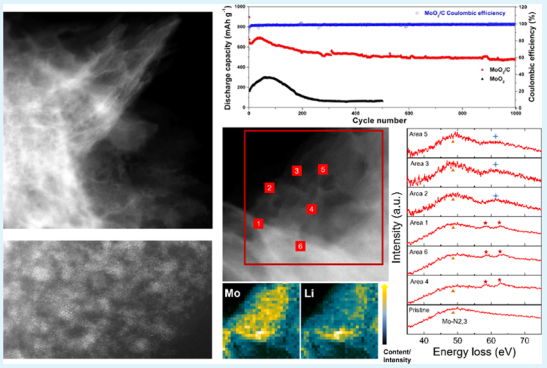

KEYWORDS: *molybdenum dioxide, carbon matrix, anode materials, nanocomposite, lithium storage mechanism*

Downloaded via WUHAN UNIV OF TECHNOLOGY on October 26, 2020 at 03:33:32 (UTC).
See https://pubs.acs.org/sharingguidelines for options on how to legitimately share published articles.

1. INTRODUCTION

Owing to energy shortage clean and sustainable energy is in urgent demand.[1−3] Featuring with high energy density and long lifespan, rechargeable lithium-ion batteries (LIBs) have dominated the power source market for portable electronics and electric vehicles. Nevertheless, the capacity of currently commercialized graphite anode is too low to meet the ever-increasing demands of energy density.[4−7] Transition metal oxides (TMOs) operated on the conversion reaction mechanism represent a promising family of high-capacity anode materials.[8] In the past decades, numerous TMOs have been widely studied, such as Fe_2O_3,[9,10] V_2O_5,[11,12] MoO_3,[13,14] and so on.[15−17] With the merits of metallic electrical conductivity, high theoretical capacity (838 mAh g^{-1}), and low cost, molybdenum dioxide (MoO_2) is considered one of the most attractive anode materials.[18−20] Nevertheless, MoO_2 usually suffers from poor kinetics and severe volume fluctuations, leading to unsatisfactory rate capability and cyclability.[21−24]

According to the previous literature,[25−27] the lithium storage process of MoO_2 is a combination of intercalation and conversion reactions

$$x\mathrm{Li}^+ + x\mathrm{e}^- + \mathrm{MoO_2} \leftrightarrow \mathrm{Li}_x\mathrm{MoO_2} (0 \le x \le 0.98) \quad (1)$$

$$\mathrm{Li}_{0.98}\mathrm{MoO_2} + 3.02\mathrm{Li}^+ + 3.02\mathrm{e}^- \leftrightarrow 2\mathrm{Li_2O} + \mathrm{Mo} \quad (2)$$

The lithium intercalation reaction of MoO_2 (eq 1) affords a quite limited capacity of 209 mAh g^{-1}, corresponding to less than one lithium per formula (eq 1).[28] The conversion reaction between Li_xMoO_2 and Mo (eq 2) can bring a high specific capacity. However, the conversion reaction is accompanied by huge volume change, resulting in poor structural stability and thus cyclability.[29−32] Besides, the conversion reaction shows poor kinetics owing to the poor conductivity of $Li_{0.98}MoO_2$. Nanostructure engineering is an effective avenue to make the conversion reaction feasible.[33] Thus, numerous studies have been conducted to synthesize

Received: June 14, 2020
Accepted: August 11, 2020
Published: August 11, 2020

ACS Publications

© 2020 American Chemical Society

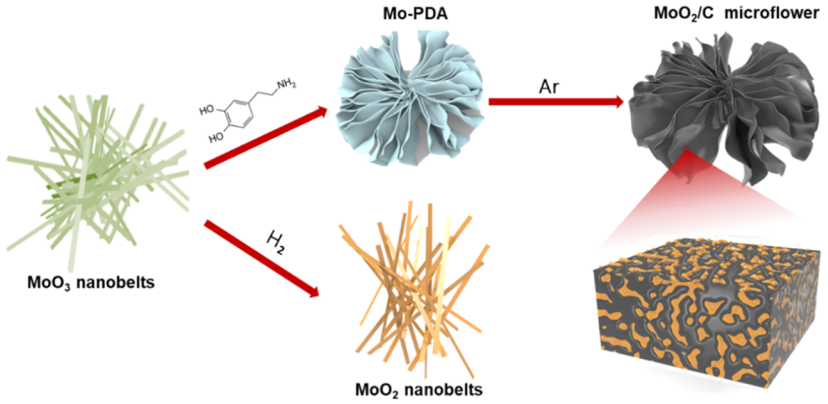

Figure 1. Schematic illustration for the fabrication of MoO_2/C and MoO_2 nanobelts.

MoO_2 nanostructures, such as nanoparticles,[29] nanorods,[25] nanosheets,[34] yolk−shell microspheres,[35] and mesoporous materials.[18] These MoO_2-based nanostructures exhibit enhanced capacities and facilitated kinetics. However, the cycle life of bare MoO_2 nanostructures is usually unsatisfactory due to the volume effects and aggregation of nanoparticles.

To improve the cyclability, efforts have been dedicated to compositing the MoO_2 with less active components, such as carbon. Chen et al. prepared MoO_2/Mo_2C heterostructured nanotubes by a one-step carbothermal reduction strategy.[24] The synthesized MoO_2/Mo_2C heterostructure demonstrated a capacity of 510 mAh g^{-1} over 140 cycles. Lou's group designed triple-shelled MoO_2/C hollow spheres, and the as-prepared MoO_2/C delivered a capacity of 580 mAh g^{-1} over 200 cycles.[36] Although the cyclability has been significantly improved by the composite strategy, it is still challenging for MoO_2-based nanocomposites to achieve a cycle life of over 1000 cycles with high capacity.

Herein, we synthesized a novel structure where ultrafine MoO_2 particles are confined within a conductive carbon nanosheet matrix (MoO_2/C). In this unique structure, the continuous carbon nanosheet matrix serves as both a conductive network and a structure supporter. It also has a strong size-confining effect to avoid the aggregation of MoO_2 particles and keep their size uniformly under 3 nm even after high-temperature calcination (800 °C in Ar). Furthermore, the ultrafine MoO_2 clusters reduce the solid diffusion lengths of Li^+, enabling favorable kinetics. With the above merits, the MoO_2/C triggers fast Li (de)intercalation and provides effective confinement of volume change during cycling. As a result, MoO_2/C shows a high capacity of 810 mAh g^{-1} at 200 mA g^{-1} and capacity retention of 75% after 1000 cycles at 1.0 A g^{-1}. Through *in situ* X-ray diffraction (XRD) analysis and *in situ* scanning transmission electron microscopy with the corresponding electron energy loss spectrum (STEM-EELS) analysis, it is demonstrated that most of MoO_2 are converted to $Li_{0.98}MoO_2$ during lithiation, and the extra lithium ions enrich to form an amorphous phase of lithium metal beside $Li_{0.98}MoO_2$ as an extra lithium storage site; a similar mechanism has been observed in ordered mesoporous MoO_2 without carbon matrix.[37] We believe this unique and hybrid lithium storage mechanism enabled by the carbon-encapsulated MoO_2 ultrafine nanoparticles can provide insight into the design of next-generation advanced electrode materials for high-performance secondary batteries with both high energy density and longevity.

2. RESULTS AND DISCUSSION

The construction of MoO_2/C is realized through a dopamine-assisted process (Figure 1). First, MoO_3 nanobelts are synthesized through a hydrothermal method according to a previous report.[38] The MoO_3 precursor shows a uniform nanobelt morphology with an average width and length of 200−250 nm and several micrometers, respectively (Figure S1). The MoO_3 nanobelts have certain solubility in H_2O and they react with dopamine hydrochloride in Tris buffer solution and go through a dissolution/redeposition/reconstruction, which leads to the formation of the organic complex, where Mo-based metal oxide clusters are embedded in a polydopamine matrix to form flower-like hierarchical-structured molybdenum−polydopamine (Mo−PDA) hybrids (Figure S2). Finally, the Mo−PDA hybrids are transformed into MoO_2/C by annealing in Ar at 800 °C. For comparison, MoO_2 nanobelts as the controlled samples are also synthesized by direct annealing the MoO_3 nanobelts in H_2/Ar.

The Mo−PDA have an average size of 2 μm. The XRD pattern of Mo−PDA (Figure S3a) resembles that of the Mo−polydopamine compound reported previously.[39] The Fourier-transform infrared spectrum (FTIR, Figure S3b) shows a series of peaks at 500−2000 cm^{-1}. The peaks at 1254, 1485, and 1598 cm^{-1} can be indexed to the bending vibrations of C−N−C, C−C═N, and N−H, respectively. The FTIR spectrum clearly demonstrates the existence of an indole structure in Mo−PDA.[39,40]

The microstructure of the synthesized samples is studied by scanning electron microscopy (SEM) and transmission electron microscopy (TEM). The MoO_2/C inherits the hierarchical flower-like morphology of Mo−PDA (Figure 2a). It is deduced that the PDA-derived carbon plays a significant role in avoiding the structural collapse during annealing. TEM images (Figure 2b) further confirm the flower-like structure of the MoO_2/C. The nanosheets as building blocks have a thickness of 10−20 nm. Numerous bright spots corresponding to the MoO_2 nanoparticles can be observed in the STEM image of such a typical nanosheet (Figure 2c). A high-resolution TEM (HRTEM, Figure 2f) image taken from the edge of the nanosheet shows that MoO_2 ultrafine particles are embedded in the amorphous carbon layer. The STEM image (Figure 2d) shows that the nanosheets are composed of a lot of thinner flakes overlapping each other. By enlarging the area on the edge of the nanosheet in Figure 2d, it can be seen that the MoO_2 nanoparticles have a size around 2 nm, as seen from the small uniform white bright spots in the image (Figure 2e). The

https://dx.doi.org/10.1021/acsami.0c10833
ACS Appl. Mater. Interfaces 2020, 12, 40648−40654

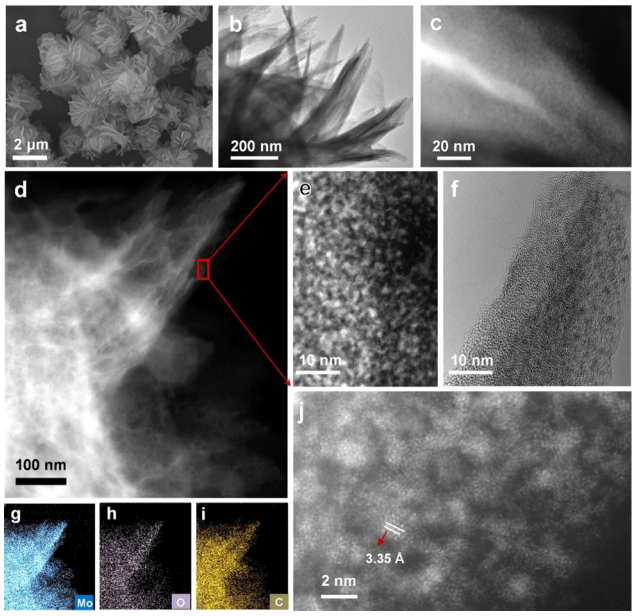

Figure 2. (a) SEM image, (b) TEM image, (c–e, j) STEM images (e is from the labeled area in d), (f) HRTEM image, and (g–i) EDS elemental mappings of MoO_2/C.

high-magnification STEM image (Figure 2j) enlarged from the area in Figure 2e demonstrates clear atomic clusters of MoO_2, and the atomic-resolution lattice distance is measured to be 3.35 Å corresponding to the (011) plane of monoclinic MoO_2, which fits well with the XRD results (Figure 3b). To figure out the elemental distribution of MoO_2/C, energy-dispersive X-ray spectroscopy (EDS) element mapping is carried out. As shown in Figure 2g–i, Mo, O, and C elements are distributed homogeneously in MoO_2/C. Based on the above analysis, we concluded that MoO_2/C is constructed by many carbon sheets composed of thinner and smaller flakes. The MoO_2 particles are ultrafine with a size of around 2 nm and embedded in the carbon sheets. The control sample, MoO_2, prepared by annealing the MoO_3 nanobelts in H_2, inherits the nanobelt morphology from MoO_3 (Figure S4). Compared to the MoO_3 nanobelts, the MoO_2 nanobelts show a shorter length and more serious aggregation.

To characterize the nature of carbon in MoO_2/C, Raman spectra are obtained (Figure 3a). The Raman spectrum of MoO_2/C shows two characteristic carbon bands at around 1356 and 1605 cm^{-1}, corresponding to the D and G bands of carbon. The other bands of MoO_2/C are similar to those of MoO_2 nanobelts, which can be ascribed to molybdenum oxides. The bands at ~234, 345, and 496 cm^{-1} are ascribed to MoO_2, and the bands at ~991, 820, and 283 cm^{-1} can be assigned to MoO_3, suggesting the surface oxidation of MoO_2.[19]

XRD patterns of both MoO_2/C and MoO_2 nanobelts can be assigned to monoclinic MoO_2 (JCPDS 65-1273) (Figure 3b).[41] No diffractions from impurities can be observed. According to the XRD patterns of the MoO_2/C, the size of MoO_2 is about 15 nm. This value is much larger than the size determined from TEM and it may be caused by the attachment of MoO_2 particles with the same specific orientation; and a similar phenomenon has been reported in previous reports.[42,43] The (011) plane of MoO_2/C, which is the strongest scattered refection in XRD, corresponds to the lattice spacing marked in Figure 2j. Compared to the MoO_2 nanobelts, MoO_2/C displays much broader diffractions, indicating the smaller crystalline size in MoO_2/C. This is because the PDA-derived carbon confines the growth of MoO_2 during carbonization.

To determine the carbon content of MoO_2/C quantitatively, thermogravimetric analysis (TGA, Figure S5) is carried out from room temperature to 700 °C in air for both MoO_2 and the MoO_2/C. The weight gain of MoO_2 is around 12 wt %, which agrees well with the theoretical value for converting MoO_2 to MoO_3. For MoO_2/C, the weight loss is 32 wt %. Considering the weight gain for the oxidation of MoO_2, the carbon content in MoO_2/C is calculated to be ~39 wt %. N_2 sorption (Figure 3c) is conducted to determine the surface area of the samples. The MoO_2 nanobelts have a moderate surface area of 15 m^2 g^{-1}. For MoO_2/C, it shows a much higher surface area of 385 m^2 g^{-1}, which is particularly beneficial for rapid Li uptake/release.

X-ray photoelectron spectroscopy (XPS) is explored to determine the surface chemical states of MoO_2 and MoO_2/C.

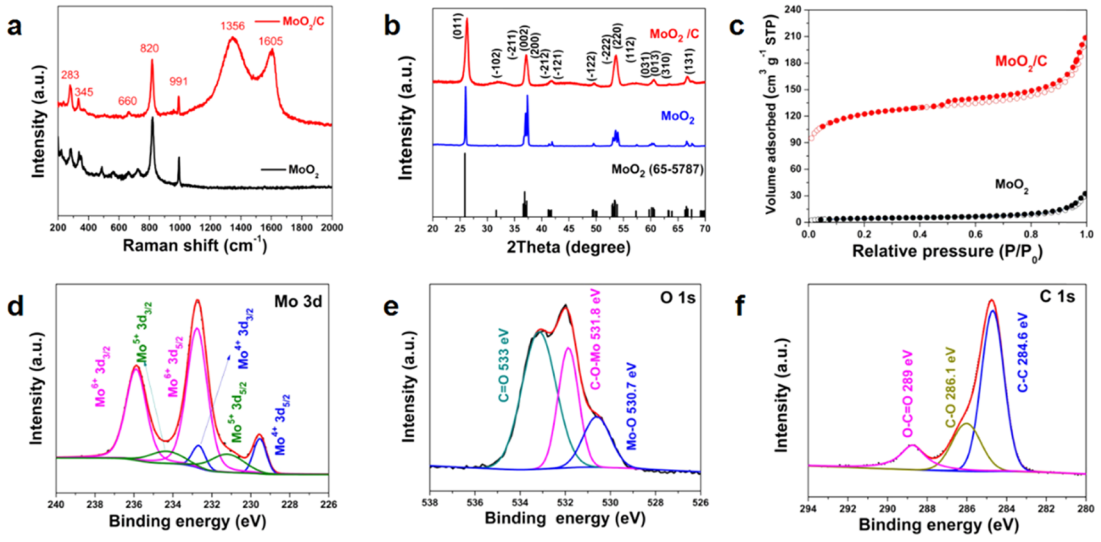

Figure 3. (a) Raman spectra, (b) XRD patterns, (c) N_2 adsorption–desorption isotherms of MoO_2 nanobelts and MoO_2/C, and (d–f) X-ray photoelectron spectra (XPS) of MoO_2/C.

https://dx.doi.org/10.1021/acsami.0c10833
ACS Appl. Mater. Interfaces 2020, 12, 40648–40654

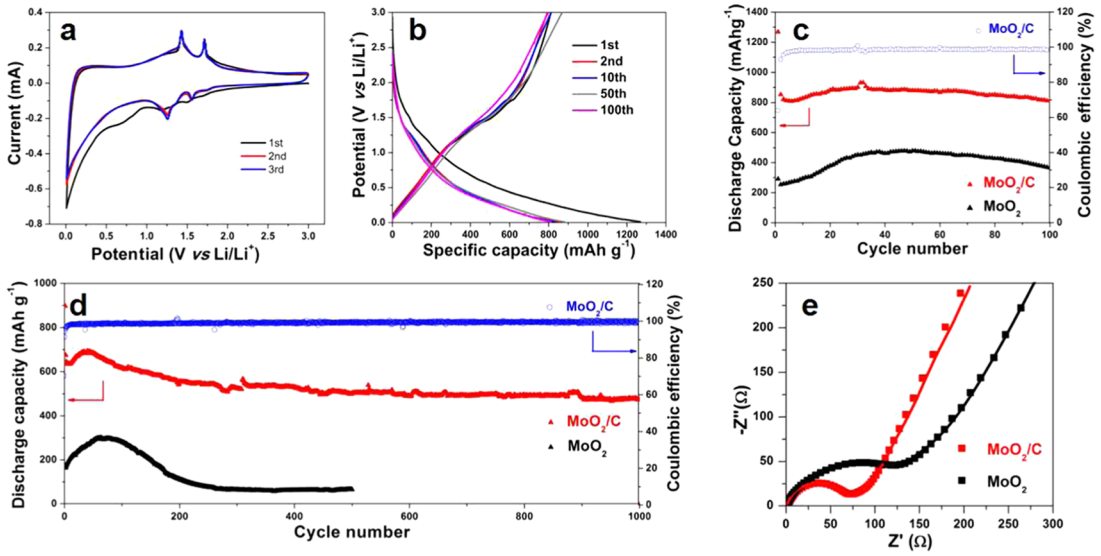

Figure 4. (a) CV curves of MoO_2/C at a scan rate of 0.2 mV s^{-1} in a potential window of 0.005−3.0 V. (b) Galvanostatic charge−discharge (GCD) curves of MoO_2/C at 200 mA g^{-1}. (c) Cycling performances of MoO_2 and MoO_2/C at 200 mA g^{-1}. (d) Long cycling performances of MoO_2 and MoO_2/C at 1.0 A g^{-1}. (e) Nyquist plots of MoO_2 and MoO_2/C.

The Mo 3d spectrum of MoO_2/C (Figure 3d) exhibits three spin−orbit doublets, which can be ascribed to Mo^{4+}, Mo^{5+}, and Mo^{6+}. The Mo^{4+} components are located at binding energies of 229.4 and 232.7 eV; the Mo^{5+} components are centered at 231.8 and 234.9 eV; the intense Mo^{6+} components are observed at 233.1 and 236.3 eV. The formation of Mo^{5+} and Mo^{6+} is caused by the partial oxidation of MoO_2.[31] For the O 1s spectrum of MoO_2/C (Figure 3e), three components at 533.6, 531.8, and 530.6 eV can be observed, corresponding to C═O, C−O−C, and Mo−O, respectively.[31,44] The C 1s spectrum (Figure 3f) of MoO_2/C exhibits three components at 288.8, 286.1, and 284.6 eV, which can be indexed to O═C−O, C−O, and C−C, respectively.[19,45]

To evaluate the electrochemical performances of MoO_2/C and MoO_2 nanobelts, coin cells are assembled. Cyclic voltammetry (CV) profiles of the MoO_2/C are shown in Figure 4a. The reduction peak at 0.6 V, which only appears in the initial cathodic process, is associated with the irreversible formation of a solid electrolyte interface (SEI) layer.[46] The first cathodic process shows two weak and broad reduction peaks at 1.17 and 1.5 V, arising from the monoclinic−orthorhombic−monoclinic phase transformations of Li_xMoO_2 induced by Li^+ intercalation.[40] Both peaks sharpen and shift toward high potentials in subsequent cycles, which is because the activation of the electrode material during initial cycling accelerates the kinetics and eases the polarization. In the anodic processes, two oxidation peaks can be observed at 1.45 and 1.72 V, corresponding to the extraction of Li^+ from lithiated Li_xMoO_2.[36] In the following cycles, the redox couples do not have apparent changes, which shows the strong stability of the structure.

Galvanostatic charge−discharge (GCD) tests are performed at 200 mA g^{-1}. MoO_2/C delivers high first discharge and charge capacities of 1268 and 842 mAh g^{-1} (Figure 4b). The irreversible capacity loss is mainly caused by the decomposition of an electrolyte and the formation of an SEI film on the electrode surface. No obvious charge/discharge plateaus can be observed in the GCD profiles. The electrochemical reactions are highly reversible, as indicated by the overlap of discharge−charge profiles after the first cycle. MoO_2/C delivers a second discharge capacity of 850 mAh g^{-1} and maintains at 810 mAh g^{-1} after 100 cycles, achieving capacity retention of ∼95% (Figure 4c). The initial Coulombic efficiency (CE) of MoO_2/C is 65%, and the CE reaches almost 100% in the following cycles (Figure 4c). For the MoO_2 nanobelts, the CV profiles show intense redox peaks, much stronger than those of MoO_2/C (Figure S6a). Two distinct charge/discharge plateaus can be discerned at 1.5/1.3 and 1.7/1.6 V in the initial 10 cycles, agreeing well with the CV results (Figure S6b). These plateaus are associated with the reversible monoclinic−orthorhombic−monoclinic phase transitions of Li_xMoO_2. The plateaus disappear gradually, owing to the pulverization of MoO_2 during successive discharge/charge. The MoO_2 nanobelts deliver first discharge and charge capacities of 298 and 220 mAh g^{-1}, giving an initial CE value of 74%. The first charge capacity is slightly over the theoretical intercalation capacity of MoO_2 (209 mAh g^{-1}), indicating the capacity is mainly contributed from eq 1. The discharge capacity of MoO_2 nanobelts increases gradually to 480 mAh g^{-1} in 30 cycles (Figure 4c), which is caused by the pulverization-induced partial conversion of Li_xMoO_2 to Mo and Li_2O.[25,26] The capacity decreases rapidly after 50 cycles and decays to 360 mAh g^{-1} after 100 cycles, indicating the unsatisfactory stability of MoO_2 nanobelts. It should be noted that each formula of MoO_2 can react with 4 Li^+, leading to a theoretic capacity of 838 mAh g^{-1}, if the conversion reaction is considered. The much lower discharge capacity of MoO_2 nanobelts may be attributed to the poor kinetics of Li_xMoO_2, which hinders the further conversion reaction.

Even at 1000 mA g^{-1}, MoO_2/C also exhibits high specific capacity and cycling stability (Figure 4d). The first and second discharge capacities are 896 and 645 mAh g^{-1}. A capacity of 480 mAh g^{-1} can be achieved over 1000 cycles with a capacity retention of ∼75%. In comparison, the MoO_2 nanobelts show much lower capacity and inferior cyclability. The capacity of MoO_2 nanobelts surges from 173 to 300 mAh g^{-1} during the first 60 cycles and it drops drastically after that. A capacity of only 65 mAh g^{-1} is retained at the 500th cycle.

Electrochemical impedance spectroscopy (EIS) is conducted to study the kinetics (Figure 4e). The Nyquist plots of both

https://dx.doi.org/10.1021/acsami.0c10833
ACS Appl. Mater. Interfaces 2020, 12, 40648−40654

samples consist of a high-frequency semicircle and a low-frequency slope line. The radius of the semicircle reflects the charge transfer resistance (R_{ct}), which is determined to be 48 Ω for MoO_2/C. This value is much lower than that of MoO_2 nanobelts (148 Ω), demonstrating the superior kinetics of MoO_2/C.

To study the rate performances, the current density is varied from 200 to 4000 mA g^{-1} (Figure S7). MoO_2/C exhibits superior rate performance, delivering average discharge capacities of about 840, 770, 710, 620, 570, and 510 mAh g^{-1} at 200, 500, 1000, 2000, 3000, and 4000 mA g^{-1}, respectively. In comparison, the MoO_2 nanobelts deliver much lower capacities.

To provide further insight into the lithium storage mechanism of MoO_2/C, *in situ* XRD is explored during discharge−charge cycling (Figure 5a). In the initial state, the

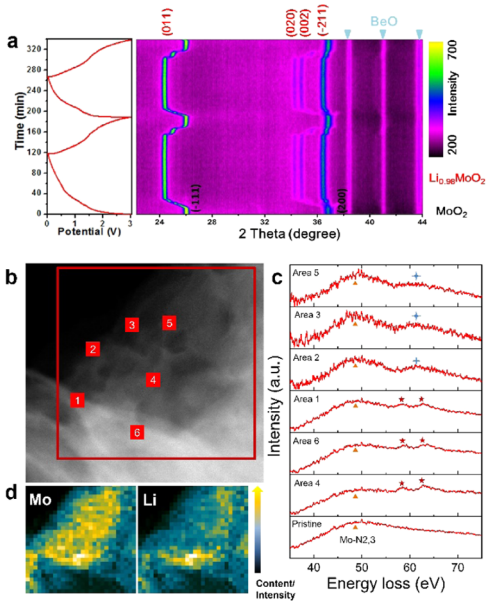

Figure 5. (a) *In situ* XRD pattern of MoO_2/C at 500 mA g^{-1}. (b) STEM of lithiated MoO_2/C. (c) STEM-EELS spectra taken from pristine MoO_2/C and areas 1−6 of the lithiated MoO_2/C. (d) Distribution of Mo and Li in lithiated MoO_2/C.

peaks located at 26.0 and 36.8° correspond to the ($\bar{1}11$) and (200) diffractions of MoO_2, while the peaks at 38.2, 40.9, and 43.6° are attributed to BeO (JCPDS 78-1564).[47] Upon initial discharge to 1.0 V, the MoO_2 diffractions shift gradually to lower angles, suggesting the lattice expansion accompanied by Li^+ insertion. Below 1.1 V, new diffraction peaks appear at 24.34, 34.4, 34.9, and 36.6°, which are ascribed to $Li_{0.98}MoO_2$ (JCPDS 84-0603).[47] When discharged to 0.01 V, the strong peaks of $Li_{0.98}MoO_2$ still remain, indicating that $Li_{0.98}MoO_2$ is the dominating lithiated product at 500 mA g^{-1}. Interestingly, the above process is fully reversible and the diffractions for MoO_2 can be recovered after the charging process. Meanwhile, the diffraction peaks of $Li_{0.98}MoO_2$ remain at 0.01 V, implying that the major capacity contribution does not come from the conversion of $Li_{0.98}MoO_2$ to Mo metal (as shown in eq 2).

To further explore its lithium storage mechanism, we performed *in situ* TEM and STEM-EELS characterizations during the lithiation process. According to the *in situ* XRD analysis results, it seems like that MoO_2/C stores lithium through the intercalation reaction. However, the achieved capacity exceeds the theoretical capacity of the intercalation reaction significantly. The *in situ* TEM video shows limited volume expansion after charging at a bias voltage of 5 V for 5 min, which is consistent with the results of *in situ* STEM and *ex situ* STEM images after the second lithiation, as shown in Figure S8. This is because of the small size of the MoO_2 particles and adequate carbon around as buffer for volume expansion. As shown in Figure 5c, *in situ* STEM-EELS spectra taken at the edge of lithiated MoO_2/C (areas 2, 3, 5) show that energy loss near the edge structures of Li species is different from those taken at other areas (areas 1, 4, and 6 correspond to the Li_xMoO_2 phase) and corresponds to metallic Li, implying that some of Li ions are accumulated as a form of metallic Li at the interface between nanosized crystalline Li_xMoO_2 domains. This shows that Li ions can be stored as either Li ion in Li_xMoO_2 or metallic Li, like that in a metallic Li battery. This result is consistent with the previous report.[37] Therefore, we conclude that during the lithiated process, a part of lithium ions is enriched at the interface between $Li_{0.98}MoO_2$ in the form of metallic lithium. It can be seen from the element distribution of Mo and Li elements that Mo is less in the edges of the nanosheets and more in the center, while the distribution of Li is basically uniform, indicating that lithium is enriched at the edges.

Based on the electrochemical characterization and *in situ* XRD and STEM-EELS results, the lithium storage processes of MoO_2 can be summarized as follows. As usual, Li^+ first intercalates into MoO_2 and yields $Li_{0.98}MoO_2$. Due to the ultrafine MoO_2 clusters' high metallic conductivity, this lithium intercalation process is highly feasible and has fast kinetics. It is also reversible for the intercalation and deintercalation. The nanopores around the oxide clusters and in the interface of the oxides and carbon matrix then provide preferential sites for the formation of the lithium-rich amorphous phase as the major Li-ion storage mechanism in further lithiation. Furthermore, the Li-metal plating in the form of amorphous compounds, $Li^+ + e^- \rightarrow Li^0$, is highly reversible in charge and discharge; thus the designed composite anode has high cyclability. As the conversion reaction is no longer the major storage mechanism, the large volumetric change due to the formation and dissociation of Li_2O is avoided, which enhances the cycling stability. Naturally, the amorphous metal Li has higher electric conductivity than Li_2O, which further improves the electrochemical performance.

3. CONCLUSIONS

In summary, a composited structure of ultrafine MoO_2 particles (<3 nm) confined by the conductive carbon nanosheet matrix (MoO_2/C) has been successfully prepared. In this unique structure, the synergistic effects of the carbon matrix and MoO_2 nanodots enable a hybrid and a highly reversible Li-ion storage mechanism, namely, the Li intercalation and the formation of the lithium-rich amorphous phase around the intercalated $Li_{0.98}MoO_2$. The flower-like carbon sheet played an important role in both the conductive network and the structure supporter with such a strong confining effect that keeps the size of MoO_2 uniformly under 3 nm even after high-temperature calcination. Moreover, good pathways for charge transfer during the cycle process are formed in the composite, which has high electron/ion conductivity and structural integrity. This unique MoO_2/C structure exhibits an excellent discharge capacity (810 mAh g^{-1} at 200 mA g^{-1}) and long cyclability (75% capacity retention

https://dx.doi.org/10.1021/acsami.0c10833
ACS Appl. Mater. Interfaces 2020, 12, 40648−40654

over 1000 cycles at 1000 mA g^{-1}). The Li-storage mechanism is confirmed by *in situ* XRD and STEM-EELS in MoO_2/C, which is a two-step reaction of an intercalation reaction followed by the formation of a metallic Li phase. This explains the intrinsic origin for such good cyclability along with high capacity. We believe this work shows a good example of how a delicate nanoscale structure design with a unique lithium storage mechanism delivers great performance and will provide insight into the design of next-generation advanced functional materials.

■ ASSOCIATED CONTENT

Supporting Information

The Supporting Information is available free of charge at https://pubs.acs.org/doi/10.1021/acsami.0c10833.

Descriptions of materials synthesis; characterization details; electrochemical measurements; the XRD pattern and FTIR for flower-like Mo−PDA composites; the SEM images of the MoO_2 nanobelts; the TGA curves of the MoO_2/C and MoO_2 nanobelts; CV curves, galvanostatic discharge−charge profiles, and rate performance of the MoO_2 nanobelts; *ex situ* STEM and *in situ* STEM images of MoO_2/C after lithiation (PDF)

In situ TEM video (AVI)

■ AUTHOR INFORMATION

Corresponding Authors

Liang Zhou − *State Key Laboratory of Advanced Technology for Materials Synthesis and Processing, Wuhan University of Technology, Wuhan 430070, China;* orcid.org/0000-0001-6756-3578; Email: liangzhou@whut.edu.cn

Jinsong Wu − *State Key Laboratory of Advanced Technology for Materials Synthesis and Processing and Nanostructure Research Centre (NRC), Wuhan University of Technology, Wuhan 430070, China;* orcid.org/0000-0002-7305-7927; Email: wujs@whut.edu.cn

Liqiang Mai − *State Key Laboratory of Advanced Technology for Materials Synthesis and Processing, Wuhan University of Technology, Wuhan 430070, China; Foshan Xianhu Laboratory of the Advanced Energy Science and Technology Guangdong Laboratory, Foshan 528200, China;* orcid.org/0000-0003-4259-7725; Email: mlq518@whut.edu.cn

Authors

Yao Yao − *State Key Laboratory of Advanced Technology for Materials Synthesis and Processing, Wuhan University of Technology, Wuhan 430070, China*

Ziang Chen − *State Key Laboratory of Advanced Technology for Materials Synthesis and Processing, Wuhan University of Technology, Wuhan 430070, China*

Ruohan Yu − *State Key Laboratory of Advanced Technology for Materials Synthesis and Processing and Nanostructure Research Centre (NRC), Wuhan University of Technology, Wuhan 430070, China*

Qiang Chen − *State Key Laboratory of Advanced Technology for Materials Synthesis and Processing, Wuhan University of Technology, Wuhan 430070, China*

Jiexin Zhu − *State Key Laboratory of Advanced Technology for Materials Synthesis and Processing, Wuhan University of Technology, Wuhan 430070, China;* orcid.org/0000-0003-1629-240X

Xufeng Hong − *State Key Laboratory of Advanced Technology for Materials Synthesis and Processing, Wuhan University of Technology, Wuhan 430070, China*

Complete contact information is available at: https://pubs.acs.org/10.1021/acsami.0c10833

Author Contributions

‖Y.Y. and Z.C. contributed equally to this work.

Notes

The authors declare no competing financial interest.

■ ACKNOWLEDGMENTS

The authors acknowledge the financial support from the National Natural Science Foundation of China (21673171, 51521001), the Shenzhen Fundamental Research Program (JCYJ20190809114409397), the National Key Research and Development Program of China (2016YFA0202603), the Program of Introducing Talents of Discipline to Universities (B17034), the Yellow Crane Talent (Science & Technology) Program of Wuhan City, and the Foshan Xianhu Laboratory of the Advanced Energy Science and Technology Guangdong Laboratory. The STEM work was performed at the Nanostructure Research Center (NRC), which is supported by the Fundamental Research Funds for the Central Universities (WUT: 2019III012GX, 2020III002GX), the State Key Laboratory of Advanced Technology for Materials Synthesis and Processing, and the State Key Laboratory of Silicate Materials for Architectures (all of the laboratories are at Wuhan University of Technology).

■ REFERENCES

(1) Liu, Y.; Zhu, Y.; Cui, Y. Challenges and Opportunities towards Fast-Charging Battery Materials. *Nat. Energy* **2019**, *4*, 540−550.

(2) Yang, C.; Chen, J.; Ji, X.; Pollard, T. P.; Lu, X.; Sun, C.-J.; Hou, S.; Liu, Q.; Liu, C.; Qing, T.; Wang, Y.; Borodin, O.; Ren, Y.; Xu, K.; Wang, C. Aqueous Li-Ion Battery Enabled by Halogen Conversion-Intercalation Chemistry in Graphite. *Nature* **2019**, *569*, 245.

(3) Zhao, Q.; Liu, X.; Stalin, S.; Khan, K.; Archer, L. A. Solid-state Polymer Electrolytes with In-Built Fast Interfacial Transport for Secondary Lithium Batteries. *Nat. Energy* **2019**, *4*, 365−373.

(4) Lin, D.; Liu, Y.; Cui, Y. Reviving the Lithium Metal Anode for High-Energy Batteries. *Nat. Nanotechnol.* **2017**, *12*, 194.

(5) Martin, C.; Genovese, M.; Louli, A.; Weber, R.; Dahn, J. Cycling Lithium Metal on Graphite to Form Hybrid Lithium-Ion/Lithium Metal Cells. *Joule* **2020**, *4*, 1−15.

(6) Shi, Y.; Liu, G.; Jin, R.; Xu, H.; Wang, Q.; Gao, S. Carbon Materials from Melamine Sponges for Supercapacitors and Lithium Battery Electrode Materials: a Review. *Carbon Energy* **2019**, *1*, 253−275.

(7) Wang, H.; Cui, Y. Nanodiamonds for Energy. *Carbon Energy* **2019**, *1*, 13−18.

(8) Zhu, J.; Tu, W.; Pan, H.; Zhang, H.; Liu, B.; Cheng, Y.; Deng, Z.; Zhang, H. Self-Templating Synthesis of Hollow Co3O4 Nanoparticles Embedded in N, S-Dual-Doped Reduced Graphene Oxide for Lithium Ion Batteries. *ACS Nano* **2020**, *14*, 5780−5787.

(9) Li, Y.; Huang, Y.; Zheng, Y.; Huang, R.; Yao, J. Facile and Efficient Synthesis of α-Fe2O3 Nanocrystals by Glucose-Assisted Thermal Decomposition Method and Its Application in Lithium Ion Batteries. *J. Power Sources* **2019**, *416*, 62−71.

(10) Zhang, L.; Wu, H. B.; Lou, X. W. D. Iron-Oxide-Based Advanced Anode Materials for Lithium-Ion Batterie. *Adv. Energy Mater.* **2014**, *4*, No. 1300958.

(11) Cao, A. M.; Hu, J. S.; Liang, H. P.; Wan, L. J. Self-assembled Vanadium Pentoxide (V2O5) Hollow Microspheres from Nanorods

and Their Application in lithium-Ion Batteries. *Angew. Chem., Int. Ed.* **2005**, *44*, 4391−4395.
(12) Liu, J.; Xia, H.; Xue, D.; Lu, L. Double-shelled Nanocapsules of V2O5-based Composites as High-performance Anode and Cathode Materials for Li Ion Batteries. *J. Am. Chem. Soc.* **2009**, *131*, 12086−12087.
(13) Du, Y.; He, J.; Hou, G.; Yuan, F. α-MoO3 Sheets with High Exposed Plane Reinforced by Thermal Plasma for Stable Li-Ion Storage. *Electrochim. Acta* **2020**, *334*, No. 135593.
(14) Zhao, X.; Jia, W.; Wu, X.; Lv, Y.; Qiu, J.; Guo, J.; Wang, X.; Jia, D.; Yan, J.; Wu, D. Ultrafine MoO3 Anchored in Coal-based Carbon Nanofibers as Anode for Advanced Lithium-Ion Batteries. *Carbon* **2020**, *156*, 445−452.
(15) He, Z.; Huang, L.-a.; Guo, J.; Pei, S.-e.; Shao, H.; Wang, J. Novel Hierarchically Branched CoC2O4@CoO/Co Composite Arrays with Superior Lithium Storage Performance. *Energy Storage Mater.* **2020**, *24*, 362−372.
(16) Li, Q.; Zhao, Y.; Liu, H.; Xu, P.; Yang, L.; Pei, K.; Zeng, Q.; Feng, Y.; Wang, P.; Che, R. Dandelion-like Mn/Ni Co-doped CoO/C Hollow Microspheres with Oxygen Vacancies for Advanced Lithium Storage. *ACS Nano* **2019**, *13*, 11921−11934.
(17) Wang, Y.; Rao, S.; Mao, P.; Zhang, F.; Xiao, P.; Peng, L.; Zhu, Q. Controlled Synthesis of Fe3O4@C@Manganese Oxides (MnO2, Mn3O4 and MnO) Hierarchical Hollow Nanospheres and Their Superior Lithium Storage Properties. *Electrochim. Acta* **2020**, *337*, No. 135739.
(18) Shi, Y.; Guo, B.; Corr, S. A.; Shi, Q.; Hu, Y.-S.; Heier, K. R.; Chen, L.; Seshadri, R.; Stucky, G. D. Ordered Mesoporous Metallic MoO2 Materials with Highly Reversible Lithium Storage Capacity. *Nano Lett.* **2009**, *9*, 4215−4220.
(19) Ma, J.; Fu, J.; Niu, M.; Quhe, R. MoO2 and Graphene Heterostructure as Promising Flexible Anodes for Lithium-Ion Batteries. *Carbon* **2019**, *147*, 357−363.
(20) Jiang, Y.; Sun, M.; Ni, J.; Li, L. Ultrastable Sodium Storage in MoO3 Nanotube Arrays Enabled by Surface Phosphorylation. *ACS Appl. Mater. Interfaces* **2019**, *11*, 37761−37767.
(21) Zhou, D.; Ni, J.; Li, L. Self-supported Multicomponent CPO-27 MOF Nanoarrays as High-Performance Anode for Lithium Storage. *Nano Energy* **2019**, *57*, 711.
(22) Hou, C.; Wang, J.; Du, W.; Wang, J.; Du, Y.; Liu, C.; Zhang, J.; Hou, H.; Dang, F.; Zhao, L.; Guo, Z. One-pot Synthesized Molybdenum Dioxide-molybdenum Carbide Heterostructures Coupled with 3D Holey Carbon Nanosheets for Highly Efficient and Ultrastable Cycling Lithium-Ion Storage. *J. Mater. Chem. A* **2019**, *7*, 13460−13472.
(23) Yun, Y.; Shao, J.; Chen, Y.; Cao, Z.; Qu, Q.; Zheng, H. Nanoisland-like MoO2 Embedded in N-Doped Carbon via Mo-N Bonds for Li-Ion Storage. *ACS Appl. Nano Mater.* **2019**, *2*, 1883−1889.
(24) Chen, Z.; Yang, T.; Shi, H.; Wang, T.; Zhang, M.; Cao, G. Single Nozzle Electrospinning Synthesized MoO2@C Core Shell Nanofibers with High Capacity and Long-Term Stability for Lithium-Ion Storage. *Adv. Mater. Interfaces* **2017**, *4*, No. 1600816.
(25) Guo, B.; Fang, X.; Li, B.; Shi, Y.; Ouyang, C.; Hu, Y.-S.; Wang, Z.; Stucky, G. D.; Chen, L. Synthesis and Lithium Storage Mechanism of Ultrafine MoO2 Nanorods. *Chem. Mater.* **2012**, *24*, 457−463.
(26) Zhang, H.-J.; Shu, J.; Wang, K.-X.; Chen, X.-T.; Jiang, Y.-M.; Wei, X.; Chen, J.-S. Lithiation Mechanism of Hierarchical Porous MoO2 Nanotubes Fabricated through One-step Carbothermal Reduction. *J. Mater. Chem. A* **2014**, *2*, 80−86.
(27) Zhao, X.; Wang, H.-E.; Cao, J.; Cai, W.; Sui, J. Amorphous/crystalline Hybrid MoO2 Nanosheets for High-energy Lithium-Ion Capacitors. *Chem. Commun.* **2017**, *53*, 10723−10726.
(28) Zhou, Y.; Xie, H.; Wang, C.; He, Q.; Liu, Q.; Muhammad, Z.; Haleem, Y. A.; Sang, Y.; Chen, S.; Song, L. Probing Lithium Storage Mechanism of MoO2 Nanoflowers with Rich Oxygen-Vacancy Grown on Graphene Sheets. *J. Phys. Chem. C* **2017**, *121*, 15589−15596.
(29) Liu, Y.; Zhang, H.; Ouyang, P.; Li, Z. One-pot Hydrothermal Synthesized MoO2 with High Reversible Capacity for Anode Application in Lithium ion Battery. *Electrochim. Acta* **2013**, *102*, 429−435.
(30) Zhu, Y.; Xu, X.; Chen, G.; Zhong, Y.; Cai, R.; Li, L.; Shao, Z. Surfactant-free Self-assembly of Reduced Graphite Oxide-MoO2 Nanobelt Composites Used as Electrode for Lithium-Ion Batteries. *Electrochim. Acta* **2016**, *211*, 972−981.
(31) Wang, P.; Zhang, Y.; Yin, Y.; Fan, L.; Zhang, N.; Sun, K. Anchoring Hollow MoO2 Spheres on Graphene for Superior Lithium Storage. *Chem. Eng. J.* **2018**, *334*, 257−263.
(32) Wang, S.; Zhang, Z.; Yang, Y.; Tang, Z. Efficient Lithium-Ion Storage by Hierarchical Core−Shell TiO2 Nanowires Decorated with MoO2 Quantum Dots Encapsulated in Carbon Nanosheets. *ACS Appl. Mater. Interfaces* **2017**, *9*, 23741−23747.
(33) Sun, Y.; Liu, N.; Cui, Y. Promises and Challenges of Nanomaterials for Lithium-based Rechargeable Batteries. *Nat. Energy* **2016**, No. 16071.
(34) Zhang, H.; Zeng, L.; Wu, X.; Lian, L.; Wei, M. Synthesis of MoO2 Nanosheets by an Ionic Liquid Route and Its Electrochemical Properties. *J. Alloys Compd.* **2013**, *580*, 358−362.
(35) Zhang, X.; Song, X.; Gao, S.; Xu, Y.; Cheng, X.; Zhao, H.; Huo, L. Facile Synthesis of Yolk−shell MoO2 Microspheres with Excellent Electrochemical Performance as a Li-Ion Battery Anode. *J. Mater. Chem. A* **2013**, *1*, 6858−6864.
(36) Wang, Y.; Yu, L.; Lou, X. W. Formation of Triple-Shelled Molybdenum−Polydopamine Hollow Spheres and Their Conversion into MoO2/Carbon Composite Hollow Spheres for Lithium-Ion Batteries. *Angew. Chem., Int. Ed.* **2016**, *55*, 14668−14672.
(37) Shon, J. K.; Lee, H. S.; Park, G. O.; Yoon, J.; Park, E.; Park, G. S.; Doo, S.; et al. Discovery of Abnormal Lithium-storage Sites in Molybdenum Dioxide Electrodes. *Nat. Commun.* **2016**, *7*, No. 11049.
(38) Zhou, L.; Zhu, J.; Yu, M.; Huang, X.; Li, Z.; Wang, Y.; Yu, C. MoxW1− x O3· 0.33 H2O Solid Solutions with Tunable Band Gaps. *J. Phys. Chem. C* **2010**, *114*, 20947−20954.
(39) Sun, L.; Wang, C.; Wang, X.; Wang, L. Morphology Evolution and Control of Mo-polydopamine Coordination Complex from 2D Single Nanopetal to Hierarchical Microflowers. *Small* **2018**, No. 1800090.
(40) Wang, C.; Sun, L.; Zhang, F.; Wang, X.; Sun, Q.; Cheng, Y.; Wang, L. Formation of Mo-Polydopamine Hollow Spheres and Their Conversions to MoO2/C and Mo2C/C for Efficient Electrochemical Energy Storage and Catalyst. *Small* **2017**, *13*, No. 1701246.
(41) Yang, L.; Sun, W.; Zhong, Z.; Liu, J.; Gao, Q.; Hu, R.; Zhu, M. Hierarchical MoO2/N-doped Carbon Heteronanowires with High Rate and Improved Long-term Performance for Lithium-Ion Batteries. *J. Power Sources* **2016**, *306*, 78−84.
(42) Fang, Y.; Hu, H. An Ordered Mesoporous Aluminosilicate with Completely Crystalline Zeolite Wall Structure. *J. Am. Chem. Soc.* **2006**, *128*, 10636−10637.
(43) Fan, W.; Snyder, M. A.; Kumar, S.; Lee, P. S.; Yoo, W. C.; McCormick, A. V.; Tsapatsis, M. Hierarchical Nanofabrication of Microporous Crystals with Ordered Mesoporosity. *Nat. Mater.* **2008**, *7*, 984−991.
(44) Bhaskar, A.; Deepa, M.; Narasinga Rao, T. MoO2/multiwalled Carbon Nanotubes (MWCNT) Hybrid for Use as a Li-Ion Battery Anode. *ACS Appl. Mater. Interfaces* **2013**, *5*, 2555−2566.
(45) Wan, J.; Wu, J.; Gao, X.; Li, T.; Hu, Z.; Yu, H.; Huang, L. Structure Confined Porous Mo2C for Efficient Hydrogen Evolution. *Adv. Funct. Mater.* **2017**, *27*, No. 1703933.
(46) Liu, T.; Lin, L.; Bi, X.; Tian, L.; Yang, K.; Liu, J.; Xu, K.; et al. In Situ Quantification of Interphasial Chemistry in Li-Ion Battery. *Nat. Nanotechnol.* **2019**, *14*, 50−56.
(47) Liu, H.; Hu, H.; Wang, J.; Niehoff, P.; He, X.; Paillard, E.; Li, J.; et al. Hierarchical Ternary MoO2/MoS2/Heteroatom-Doped Carbon Hybrid Materials for High-Performance Lithium-Ion Storage. *ChemElectroChem* **2016**, *3*, 922−932.

https://dx.doi.org/10.1021/acsami.0c10833
ACS Appl. Mater. Interfaces 2020, 12, 40648−40654